BIOCHEMISTRY

Genome-wide in vivo screen of circulating tumor cells identifies *SLIT2* as a regulator of metastasis

Fan Xia[1]†, Yuan Ma[1,2]†, Kangfu Chen[1], Bill Duong[3], Sharif Ahmed[1], Randy Atwal[1,4], David Philpott[5], Troy Ketela[6], Jennifer Pantea[1], Sichun Lin[7], Stephane Angers[1,7,8]*, Shana O. Kelley[1,3,4,9,10]*

Circulating tumor cells (CTCs) break free from primary tumors and travel through the circulation system to seed metastatic tumors, which are the major cause of death from cancer. The identification of the major genetic factors that enhance production and persistence of CTCs in the bloodstream at a whole genome level would enable more comprehensive molecular mechanisms of metastasis to be elucidated and the identification of novel therapeutic targets, but this remains a challenging task due to the heterogeneity and extreme rarity of CTCs. Here, we describe an in vivo genome-wide CRISPR knockout screen using CTCs directly isolated from a mouse xenograft. This screen elucidated *SLIT2*—a gene encoding a secreted protein acting as a cellular migration cue—as the most significantly represented gene knockout in the CTC population. *SLIT2* knockout cells are highly metastatic with hypermigratory and mesenchymal phenotype, resulting in enhanced cancer progression in xenograft models.

INTRODUCTION

Metastasis accounts for more than 90% of deaths from cancer yet remains poorly understood and largely incurable (*1–3*). Despite advances in cancer treatment that substantially reduce morbidity and mortality of various cancer types, metastasis still leads to poor prognosis of patients with cancer and treating metastasis remains a tremendous challenge (*4, 5*). To develop more effective therapies and improve patient outcomes, further progress elucidating the fundamental biology of metastasis is critical to reveal mechanisms at the molecular level and provide insights regarding new therapeutic targets. Comparing the genetic background between primary tumors and metastatic lesions using whole-exome sequencing (WES) and whole-genome analyses has facilitated the identification of genetic factors that drive tumor progression and dissemination (*6, 7*). However, deciphering drivers of metastasis solely on the basis of the genetic information from solid tumors is limiting because of genetic divergence and tumor heterogeneity (*7–9*).

As circulating tumor cells (CTCs) leave primary tumors and seed metastatic lesions, molecular characterization of CTCs is critical to facilitate comprehensive understanding of the metastatic processes. Progress in the area of CTC enrichment and single-cell sequencing technologies has enabled identification of CTC-specific mutations in patients with cancer at the genomic level (*10–12*). However, efficient capture of CTCs and their unbiased genomic amplification for WES are still challenging because of the rarity and fragility of CTCs (*11–16*). In addition, particular mutations observed in individual patient CTCs could be anecdotal, with low applicability and weak prognostic potential for large patient populations. Thus, new technologies and platforms are needed to comprehensively and systematically study the genetic factors underlying the CTC phenotypes that contribute to the metastatic process.

Here, we report a genome-wide CRISPR knockout (KO) screen designed to identify genes contributing to CTC dissemination in vivo. Xenografted tumors were seeded with pools of CRISPR-edited cells with each cell having loss of function of one gene in the human genome. Using a high-performance approach for CTC capture directly from blood coupled with next-generation sequencing (NGS) of barcoded single-guided RNAs (sgRNAs), we identified gene KOs that promoted CTC abundance. This approach allowed the systematic identification of possible metastasis-promoting genetic factors at the CTC level with minimal bias. Previous genome-wide in vivo CRISPR screens identifying metastatic factors primarily used solid tumors or CTCs cultured ex vivo (*17, 18*). Our approach, however, allowed genome-wide in vivo CRISPR screening to be performed on fresh CTCs directly collected from liquid biopsy without extensive culturing. Avoiding ex vivo culturing of CTCs is important to prevent possible changes in morphology and proliferation of CTC subpopulations (*19, 20*), which could affect representations of subsets of sgRNAs in the library. Our in vivo CTC CRISPR KO screen elucidated Slit Guidance Ligand 2 (SLIT2) as a secreted factor that promoted the epithelial-to-mesenchymal transition (EMT) of tumor cells, resulting in enhanced intravasation. *SLIT2* KO cells had increased expression of complex I and were hypersensitive to the treatment of complex I inhibitor rotenone. Loss of *SLIT2* increased CTC numbers and the extent of metastasis of prostate cancer in an animal model.

RESULTS

Genome-wide in vivo CRISPR-Cas9 KO screen on CTCs

Genome-wide CRISPR screens are powerful tools for the systematic and unbiased identification of genes involved in metastasis (*17, 18, 21*). Combining a CRISPR-Cas9 genome-wide editing system (TKOv3: Toronto KnockOut version 3 CRISPR library) (*22*) and a high-throughput immunomagnetic microfluidic device for rare

[1]Department of Pharmaceutical Sciences, Leslie Dan Faculty of Pharmacy, University of Toronto, Ontario, Canada. [2]Key Laboratory of Tribology, Tsinghua University, Beijing 100084, P.R. China. [3]Department of Chemistry, University of Toronto, Toronto, Ontario, Canada. [4]Department of Biochemistry and Molecular Genetics, Northwestern University, Chicago, IL, USA. [5]Department of Electrical and Computer Engineering, University of Toronto, Toronto, Ontario, Canada. [6]Princess Margret Genomics Centre, University Health Network, Toronto, Ontario, Canada. [7]Donnelly Centre for Cellular & Biomolecular Research, Temerty Faculty of Medicine, University of Toronto, Toronto, ON, Canada. [8]Department of Biochemistry, Temerty Faculty of Medicine, University of Toronto, ON, Canada. [9]Department of Chemistry, Northwestern University, Evanston, IL, USA. [10]Department of Biomedical Engineering, Northwestern University, Evanston, IL, USA.
*Corresponding author. Email: shana.kelley@northwestern.edu (S.O.K.); stephane.angers@utoronto.ca (S.A.)
†These authors contributed equally to this work.

cell enrichment (*23*, *24*), we systematically investigated genes promoting CTCs and tumor progression (Fig. 1A and fig. S1A). The in vivo genome-wide loss-of-function CRISPR-Cas9 screen was conducted using the prostate cancer cell line PC-3M as a model of tumor progression. After subcutaneous injection of the TKOv3-edited cancer cells ($n = 3.0 \times 10^7$ cells injected per animal) into the immunodeficient mice ($n = 6$ mice), tumor growth from the TKOv3-transduced PC-3M cells was monitored and compared to the tumor size resulted from the parental PC-3M cells ($n = 3$ mice, 3.0×10^7 cells injected per animal) for 3 weeks. No significant differences in the size of the primary tumors between these two groups were observed (Fig. 1B). At a predefined end point of 3 weeks, whole blood was collected from each animal to isolate CTCs for sgRNA enrichment analysis. Efficient isolation of CTCs from whole blood was accomplished by the immunomagnetic labeling of the epithelial marker epithelial cell adhesion molecule (EpCAM) on the cell surface and magnetic deflection of CTCs away from blood cells using metglas tracks embedded in a

microfluidic chip (fig. S1, A and B) (*24*). CTCs collected were lysed (*25*) to obtain genomic DNA for the amplification of sgRNA regions using polymerase chain reaction (PCR) and the determination of each sgRNA abundance using NGS analysis (fig. S1C). CTC sgRNA counts were successfully obtained for all the six mice tested using our in vivo CTC CRISPR screening pipeline, with consistent total sgRNAs counts across replicates as detailed below.

For sgRNA enrichment analysis, we first analyzed the TKOv3 library attrition across the initial CRISPR-edited PC-3M cells, the primary tumors, and the isolated CTCs. Compared to the sgRNA counts in the initial TKOv3-transduced PC-3M cell pool before injection, most of the sgRNAs from the library had significantly reduced or no representation in the isolated CTC samples (Fig. 1, C and D). Given that 30 million cells (each contained 1 sgRNA) were xenografted and a library size of 71,090 sgRNAs, an initial 400× representation of the TKOv3 library was obtained. With a median capture of 100 CTCs per animal, a drastic library attrition at the CTC level
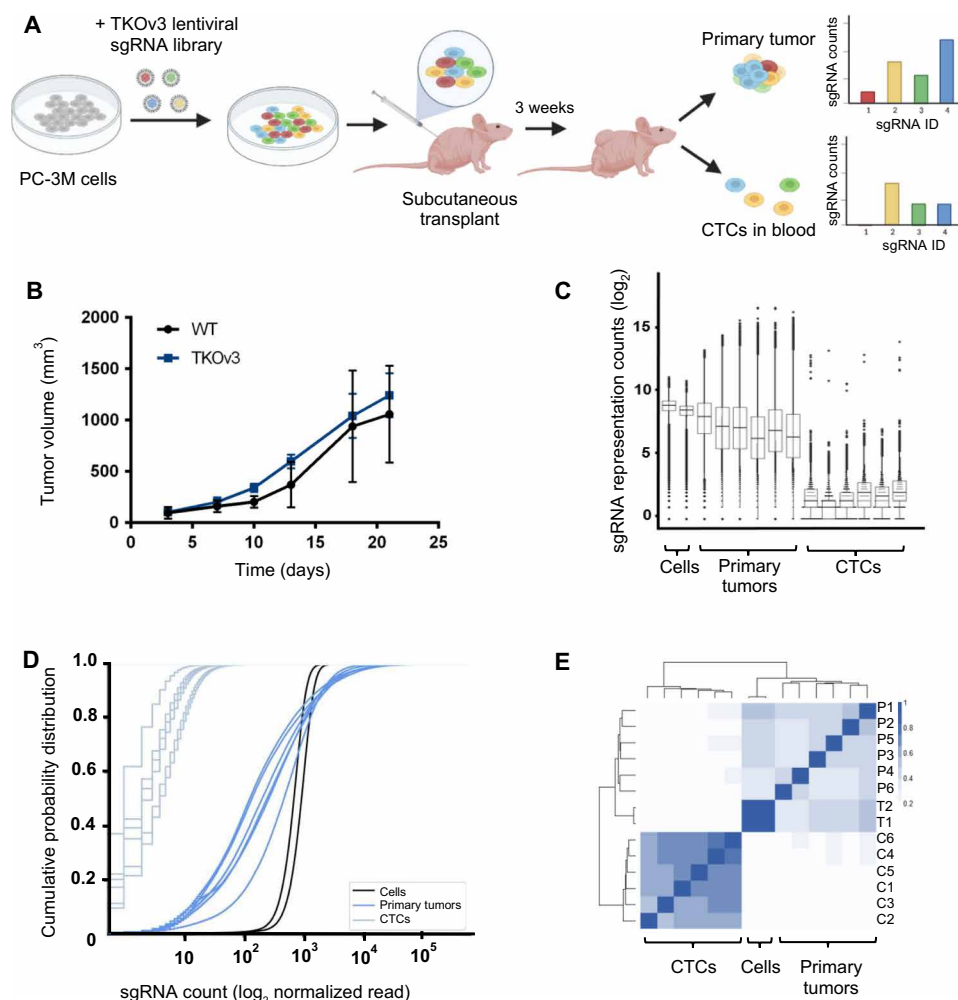

Fig. 1. An in vivo genome-wide CRISPR-Cas9 KO screen identifying CTC-promoting genetic factors. (**A**) Experimental design of the genome-wide CRISPR-Cas9 KO screen focused on CTCs. (**B**) Primary tumor growth curves of the immunocompromised mice subcutaneously transplanted with either the TKOv3-transduced PC-3M cells or the control cells ($n = 3$ for each group). Error bars indicate SD. WT, wild type. (**C**) Box plot of the sgRNA counts from the TKOv3-transduced cell pool before transplantation (cells), primary tumors, and CTCs. (**D**) Cumulative probability distribution of sgRNA counts from the TKOv3-transduced cell pool before transplantation (cells, $n = 2$), primary tumors ($n = 6$), and CTCs ($n = 6$). (**E**) Pearson correlation coefficient of the sgRNA counts from the TKOv3-transduced cell pool before transplantation (Tn), primary tumors (Pn), and CTCs (Cn).

was expected. Notably, the reduction of the sgRNA representation was much less in the primary tumor samples because substantially more cells and input materials were available for NGS (Fig. 1, C and D, and fig. S2A). In addition, the overall distribution of sgRNAs in the CTC samples clustered tightly with each other and formed a clade distinct from the sgRNAs representing the CRISPR-edited PC-3M cells and primary tumor samples (Fig. 1E). When individual sgRNA enrichment was examined for the primary tumors, a clear trend emerged with the top-ranked genes representing well-established tumor suppressor genes (TSGs) such as *TSC1* (table S1) (*26*, *27*). Frequent loss-of-function mutations of the top gene hits were also observed in patient tumor data collected from the Catalogue Of Somatic Mutations In Cancer (COSMIC) with copy number variation analysis (fig. S3) (*17*, *28*, *29*).

Selection of top enriched sgRNAs in CTCs

To analyze the CTC-enriched sgRNAs, we developed two selection criteria for robust candidate hit identification (Fig. 2, A and B). In the first selection criterion, we took into account the expected number of CTCs captured at the time of sample harvesting (median CTC count 100 per mouse). As a result, only the top 100 sgRNA counts from each of the six replicates were pooled together (600 sgRNAs × 6 replicates) to generate a list of 162 unique sgRNAs (Fig. 2A). The number of sgRNAs selected using this criterion was 162 instead of 600 due to the exclusion of the repetitive sgRNAs among the six replicates. The second criterion prioritized sgRNAs that were consistently enriched in CTC samples harvested across all the six mice injected compared to their tumor sample counterpart. sgRNAs that were enriched in five or less replicates were excluded from the selection. This resulted in the identification of 149 unique sgRNAs that were enriched across all the CTC samples compared to their corresponding primary tumors (Fig. 2B). After filtering for sgRNAs that satisfied both selection criteria (overlapping sgRNA from the two selection criteria), the final CTC sgRNA enrichment list consisted of 38 unique sgRNAs, and the genes targeted by these sgRNAs were selected for downstream analysis (Fig. 2, C and D). The biological
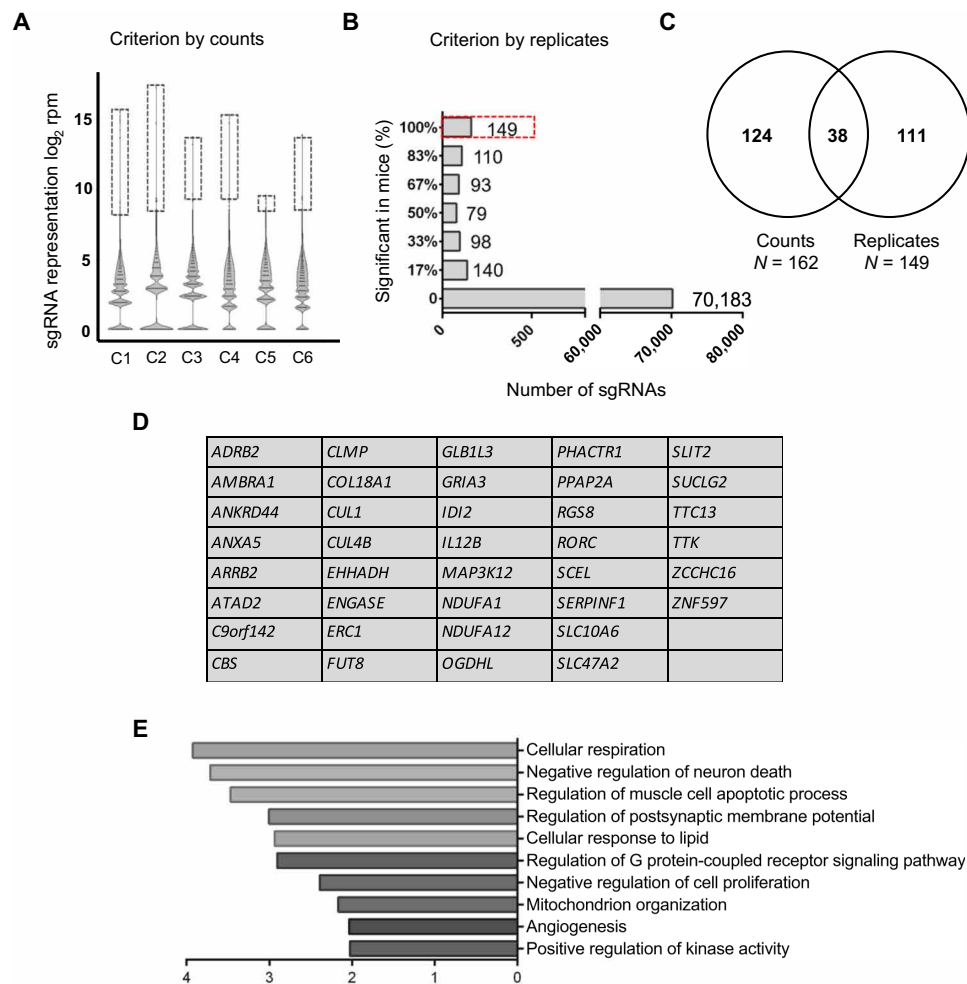

Fig. 2. Identification of top hits from the genome-wide CRISPR-Cas9 KO screen. (**A**) Violin plots of the top 100 sgRNA counts from the six CTC samples (C1 to C6). The dashed boxes highlight the top 100 sgRNA counts from each CTC sample. (**B**) Frequency (percentage of mice) of each sgRNA being enriched in CTCs compared to the corresponding primary tumors. The dashed box highlights the 149 sgRNAs enriched in CTCs across all six mice. (**C**) Venn diagram showing selection of the top-enriched sgRNAs from the CTC samples. Thirty-eight sgRNAs satisfied both the "counts" criterion in (A) and the "replicates" criterion in (B), and their targeted genes were selected for downstream analysis. (**D**) List of the 38 genes selected for the construction of the sublibrary. (**E**) Biological pathways being enriched from the 38 genes selected. Analysis and image preparation were conducted by Metascape.

pathways represented by these 38 genes were found to be highly related to metastatic processes such as the regulation of apoptosis and cell proliferation (Fig. 2E). Because no more than one sgRNA was enriched for each of the 38 genes selected from the genome-wide screen, we designed a subpool CRISPR KO library to functionally validate the top hits from the initial genome-wide screen, and a true top hit must have multiple sgRNAs present in the top enriched sgRNA list generated from the subpool screen.

Functional validation of top hits with sublibrary screen

A customized subpool CRISPR KO library consisting of 400 sgRNAs specifically targeting the 38 genes of interest (10 sgRNAs per gene) plus 20 nontargeted control (NTC) sgRNAs was generated. CRISPR-edited PC-3M cells using the subpool library were xenografted using an analogous protocol to the original screen, including the number of mice used ($n = 6$ mice) and the number of cells injected ($n = 3.0 \times 10^7$ cells injected per animal) (fig. S1D). CTC capture was improved by viral transducing the Glycosylphosphatidylinositol (GPI)–anchored Myc-tag into PC-3M cells before the subpool screen, allowing Myc-based immunomagnetic capture of CTCs (fig. S1B). As observed previously, compared to the other sample groups (plasmid pool, infected cells before transplant, and primary tumors), the number

of unique sgRNAs with significant representation in the total sgRNA reads was markedly reduced for the CTCs (Fig. 3A and fig. S2B). Notably, reads for the sgRNAs targeting *SLIT2* accounted for 10% of the total sgRNA counts in the CTC samples, with 4 of the 10 sgRNAs targeting *SLIT2* highly represented in the CTC population (Fig. 3B). Accordingly, *SLIT2* KO was ranked to be the most significant loss-of-function mutation that appeared to increase the number of CTCs, with a much higher ranking score than the rest of the genes tested in the sublibrary (Fig. 3C). *SLIT2* was thus selected for downstream analysis.

Loss of *SLIT2* is associated with poor prognosis of patients with prostate cancer and induced metastasis in vivo

SLIT2 belongs to a family of secreted proteins with a known role in axon guidance through interaction with the Roundabout family of receptors (30, 31). *SLIT2* was also found to be expressed in various cancer tissues with context-dependent promotion or inhibition of cancer progression (32–34). However, no previous studies had focused on the expression of *SLIT2* in CTCs and the effect of this genetic factor on generation of CTCs, especially in a context of prostate cancer. In the light of our CTC CRISPR KO screen conducted with the prostate cancer cell line PC-3M, we hypothesized
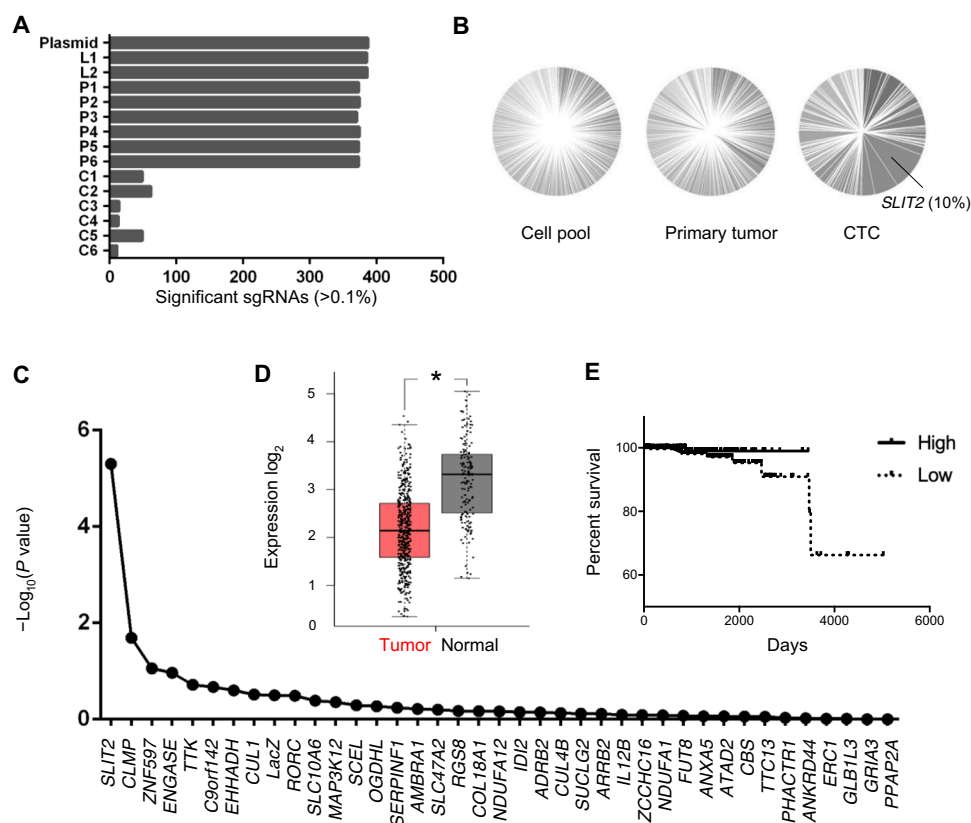

Fig. 3. Loss of *SLIT2* was a key factor of CTC production in the subpool screen and was associated with poor prognosis of patients with prostate cancer. (**A**) Bar graph of the number of significant sgRNAs (counts > 0.1% of total reads) from the plasmid library (plasmid), the initial cell pool before transplant (L*n*), primary tumors (P*n*), and CTCs (C*n*) of the sublibrary CRISPR KO screen. (**B**) Pie chart showing gene enrichment (percentage of total reads) of the initial cell pool, primary tumor, and CTC samples from the subpool CRISPR KO screen. (**C**) Gene ranking from the subpool CRISPR KO screen. *SLIT2* KO was found to be the most abundant gene KO present in CTCs. (**D**) *SLIT2* expression levels in tumor and normal tissues of patients with prostate adenocarcinoma (PRAD) were compared using RNA sequencing data collected from TCGA and prepared by GEPIA2 (tumor, $n = 492$; normal, $n = 152$). *P* value cutoff was set to be 0.01, *P < 0.01. (**E**) Survival plot of patients with PRAD with low or high expression of *SLIT2*. Data were collected from TCGA, with an expression cutoff at 2.45 FPKM (high expression, $n = 189$; low expression, $n = 305$).

that *SLIT2* negatively regulates CTC production and thereby prevents metastatsis.

On the basis of patient data collected from The Cancer Genome Atlas (TCGA), *SLIT2* expression level is significantly reduced in tumor tissues compared to normal prostate tissues (Fig. 3D). Low *SLIT2* expression is also associated with poor prognosis and overall survival of patients with prostate cancer (Fig. 3E). In addition, reduced expression of *SLIT2* in tumor tissues compared to the corresponding normal tissues is observed in 26 of the 31 human cancers recorded in TCGA (fig. S4), indicating the generality of the negative correlation between *SLIT2* expression and development of tumors.

To investigate the role of *SLIT2* in a prostate cancer model, we generated *SLIT2* KO PC-3M cells using CRISPR editing to probe the effects of losing this gene in vivo (fig. S5A). Equal numbers of NTC or the *SLIT2* KO PC-3M cells (1×10^6) were orthotopically injected into the prostate of immunodeficient mice. At the end point of tumor growth, the number of CTCs present in the whole blood of the mice injected with *SLIT2* KO cells was increased up to fivefold compared to the group injected with the NTC cells (Fig. 4A and fig. S5, D and E). The xenograft generated from *SLIT2* KO cells also exhibited enhanced proliferation of cancer cells, resulting in significantly increased tumor size compared to the control group (fig. S5, B and C). To assess whether the enhanced CTC production in *SLIT2* KO model was solely because of elevated tumor size, *SLIT2* KO xenografts with comparable tumor sizes to the control were generated with a decreased number of *SLIT2* KO cells at injection (Fig. 4B). In this case, *SLIT2* KO again exhibited a significantly increased number

of CTCs in whole blood compared to the control group (Fig. 4B), indicating enhanced intravasation and dissemination of cells lacking *SLIT2*. Because less cells were used for injection and blood samples were harvested earlier in this case to ensure comparable tumor sizes between control and *SLIT2* KO cells, overall CTC counts were lower compared to the previous injection. In addition, severe infiltration of neoplastic cells was observed inside the lymph nodes of the *SLIT2* KO models, with cases of subcapsular and intravascular invasion found in multiple hematoxylin and eosin (H&E)–stained histology sections (Fig. 4, C and D, and fig. S5F). No invasion or peripheral infiltration of neoplastic cells was observed for the prostate cancer model generated from the control cells at the time of harvest. Lymph node was used as a representation of metastasis model based on our previous observation that PC-3M had more chances to develop metastasis at the lymph nodes at late metastatic stage compared to other prostate cancer cell lines such as LNCaP (*35*). We concluded that KO of *SLIT2* promotes CTC numbers and thereby increases metastatic burden in a prostate cancer model.

Loss of *SLIT2* results in enhanced migratory and invasive behavior of prostate cancer cells

To understand mechanisms by which *SLIT2* modulates the metastatic process, we studied *SLIT2* KO and NTC cells using a variety of phenotypic assays to assess cell proliferation, deformability, and invasion. Three-dimensional (3D) spheroids cultured from the *SLIT2* KO and the NTC cells were comparable in size and composed of similar number of cells, but the *SLIT2* KO spheroids appeared to be
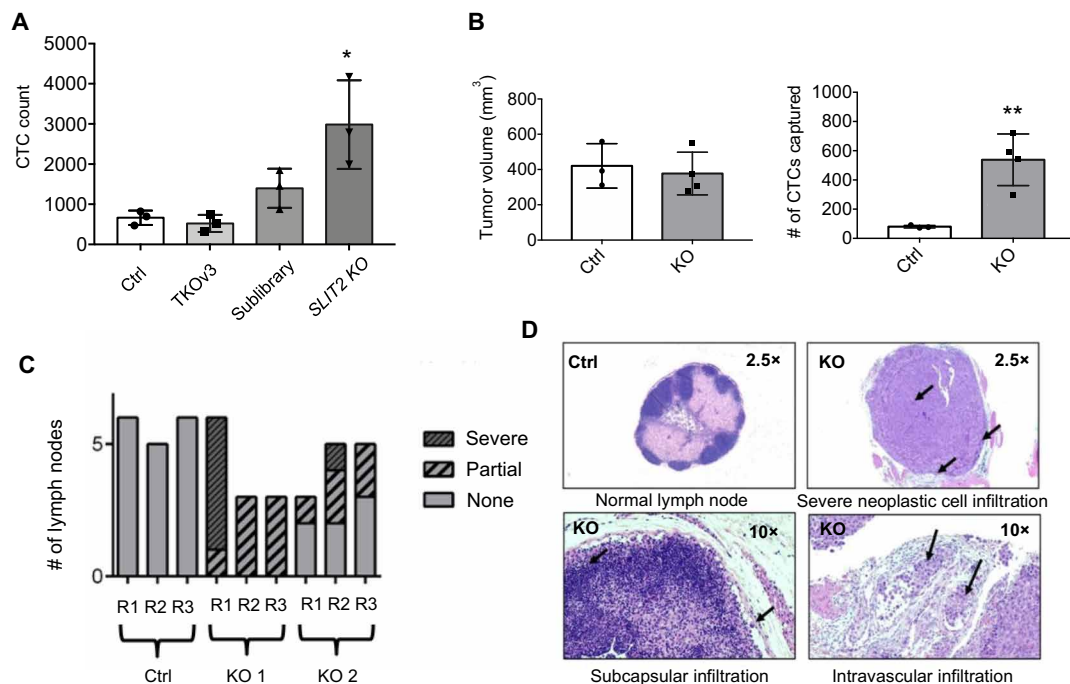

Fig. 4. *SLIT2* KO promoted cancer progression in vivo. (**A**) Bar graph of the number of CTCs counted from the whole blood of the immunocompromised mice after transplant of NTC, genome-wide CRISPR KO library (TKOv3), TSG-enriched CRISPR KO sublibrary, or *SLIT2* KO cells (*n* = 3 for each group). Error bars indicate SD. *P* value was calculated by two-tailed unpaired *t* test. **P* = 0.045. (**B**) Bar graph comparing CTC number resulted from similar tumor size of NTC and *SLIT2* KO cells (*n* = 3 for each group). KO group had one additional sample. Error bars indicate SD. *P* value was calculated by two-tailed unpaired *t* test. ***P* = 0.0072. (**C**) Bar graph of the number of lymph nodes with normal, neoplastic cell–infiltrated, and severely infiltrated tissues. Histology slides were prepared from lymph nodes collected from the immunocompromised mice after orthotopic injection of either NTC or the two *SLIT2* KO cell lines. (**D**) Representative images of the H&E-stained sections showing normal lymph node tissues (upper left) (Ctrl), as well as severe (upper right), subcapsular (bottom left), and intravascular (bottom right) neoplastic cell infiltration (*SLIT2* KO).
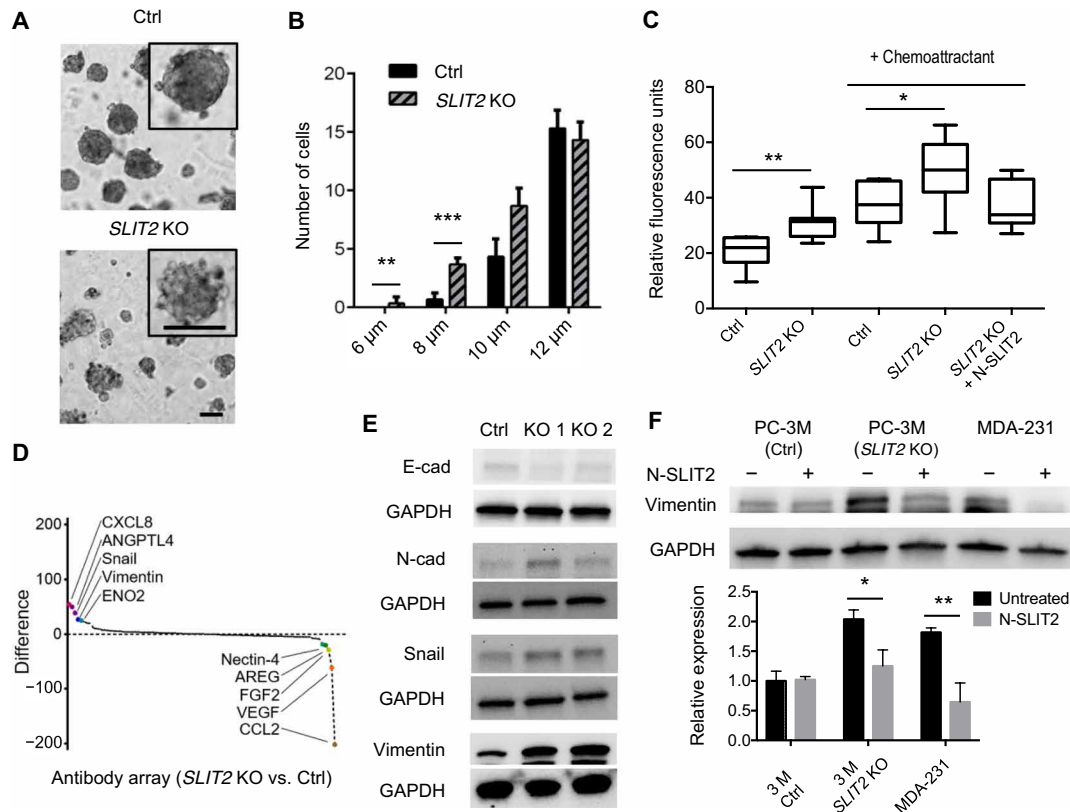
Fig. 5. *SLIT2* KO facilitated metastasis with activation of EMT. (**A**) Representative images of the spheroids formed from NTC or *SLIT2* KO PC-3 M cells. The scale bar represents length of 100 μm. (**B**) Bar graph comparing the number of deformed NTC versus *SLIT2* KO cells at different migration channel widths ($n = 3$ for each group). (**C**) Box plot comparing the number of NTC versus *SLIT2* KO cells invaded across the Transwell membrane with or without the presence of the chemoattractant or N-SLIT2 protein in the culture media ($n = 8$ for each group). (**D**) Proteins ranked on the basis of levels of differential expression in *SLIT2* KO compared to NTC cells as detected by the oncology antibody array. (**E**) Immunoblots detecting E-cadherin, N-cadherin, Snail, and Vimentin expression in *SLIT2* KO and NTC cells. GAPDH, glyceraldehyde-3-phosphate dehydrogenase. (**F**) Immunoblots detecting Vimentin protein levels in control and *SLIT2* KO PC-3M, as well as MDA-231 cells, either with or without supplementation of N-SLIT2 protein in culture medium. Error bars indicate SD. P values were calculated by two-way analysis of variance (ANOVA), except for (C) which was by two-tailed unpaired t test. ***$P < 0.001$; **$P < 0.01$; *$P < 0.05$.

poorly organized with cells on the outer surface of the spheroids being loosely attached (Fig. 5A and fig. S6). To evaluate the impact of *SLIT2* loss of function on the migratory potential of PC-3M cells, we designed a specialized microfluidic device with migration channels connecting the cell-loading and the nutrient-holding pools (fig. S7). The channels had a constant height of 5 μm but decreasing width, thereby requiring the cells to undergo remodeling to squeeze through narrowing channels toward the nutrients (fig. S7). While a comparable number of *SLIT2* KO and NTC cells traveled through the migration channels wider than 10 μm, significantly more *SLIT2* KO cells were able to fit into the channels of width 8 μm or less (Fig. 5B and fig. S7B).

The invasive behavior of *SLIT2* KO and control cells was also tested using a Transwell cell invasion assay. A larger number of *SLIT2* KO cells migrated from the top to the bottom of the membrane compared to the control group, with or without the presence of the chemoat-tractant in the lower chamber (Fig. 5C). The number of invading *SLIT2* KO cells was similar to that of control cells when the media was supplemented with exogenous SLIT2 protein (Fig. 5C). Results of cell deformability and invasion assays were independent of cell prolif-eration rates, as no significant difference between the cell numbers of control and *SLIT2* KO was found after 2D culturing for 3 days (fig. S8).

Loss of *SLIT2* results in activation of EMT

The interrogation of a panel of cancer-related proteins using an on-cology antibody array revealed several strong hits that connected the migratory and invasive phenotypes observed in *SLIT2* KO cells to the EMT (Fig. 5D and fig. S9). Considering the most elevated pro-tein family or biological pathways identified from the array, protein levels of both mesenchymal markers Vimentin and Snail were en-hanced in *SLIT2* KO cells. Thus, we hypothesized that the KO pro-duced a more mesenchymal phenotype. Reduced expression of the epithelial marker (E-cadherin) and increased expression of mesen-chymal markers (Vimentin, N-cadherin, and Snail) were observed for *SLIT2* KO cells compared to NTC cells, indicating that EMT may be linked to the metastatic phenotype of cells lacking *SLIT2* (Fig. 5E and fig. S10). Expression level of the epithelial marker EpCAM on the cell surface was also checked as it was used for the CTC capture during the screening process, and no significant difference was found comparing control and *SLIT2* KO cells (fig. S11).

Reversal of the mesenchymal phenotype was explored in a rescue experiment where exogenous SLIT2 was added to culture media, and the level of Vimentin was analyzed. Addition of SLIT2 did not have a significant effect on Vimentin expression in control PC-3M cells (Fig. 5F and fig. S12). However, the level of Vimentin in *SLIT2*

KO PC-3M cells, which was originally doubled compared to that of the control cells, was significantly reduced with the addition of exogenous SLIT2 (Fig. 5F and fig. S12). In addition, we also tested Vimentin levels for a metastatic breast cancer cell line (MDA-MB-231), and significant decrease of Vimentin expression was observed with the presence of SLIT2 (Fig. 5F and fig. S12), extending the link between *SLIT2* and EMT in a different context.

Loss of *SLIT2* resulted in elevated complex I expression with hypersensitivity to rotenone

To elucidate additional drivers of the invasive phenotype of *SLIT2* KO cells, we also performed gene expression profiling of NTC and *SLIT2* KO cells (Fig. 6, A and B). Notably, *SLIT2* KO cells exhibited increased expression of one component of the ATP synthase (*ATP6*) and multiple subunits of the complex I (*MT-ND1*, *MT-ND2*, and *MT-ND5*) belonging to the mitochondrial electron transport chain (ETC), making metabolic process and oxidative phosphorylation the most enriched gene ontology term (Fig. 6B and fig. S13). Elevated expression of ETC components suggested a possible dependency of *SLIT2* KO cells on mitochondrial activity and oxidative metabolism.

Confirming this prediction, *SLIT2* KO cells were significantly more sensitive to treatment with the complex I inhibitor rotenone when compared to the control cells (Fig. 6C). To test whether the elevated activity of complex I contributed to the increased migratory potential of the PC-3M cells lacking *SLIT2*, we tested the ability of rotenone to block migration of *SLIT2* KO and control cells using the microfluidic device described above (fig. S7). Upon treatment of rotenone, significant reduction of the number of deformed cells was observed in both groups at wider channel width (Fig. 6D). However, for the narrower channels, rotenone was more effective in inhibiting the migration of the *SLIT2* KO cells than on the NTC cells (Fig. 6D). Other two prostate cancer cell lines LNCaP and PC3 also showed enhanced sensitivity to rotenone with *SLIT2* being knocked out (figs. S14 and S15). Treatment of rotenone significantly reduced the enhanced invasiveness of LNCaP and PC3 with *SLIT2* KO (fig. S16).

DISCUSSION
Previous studies of the role of *SLIT2* in metastasis have produced contradictory observations in different experimental systems, with
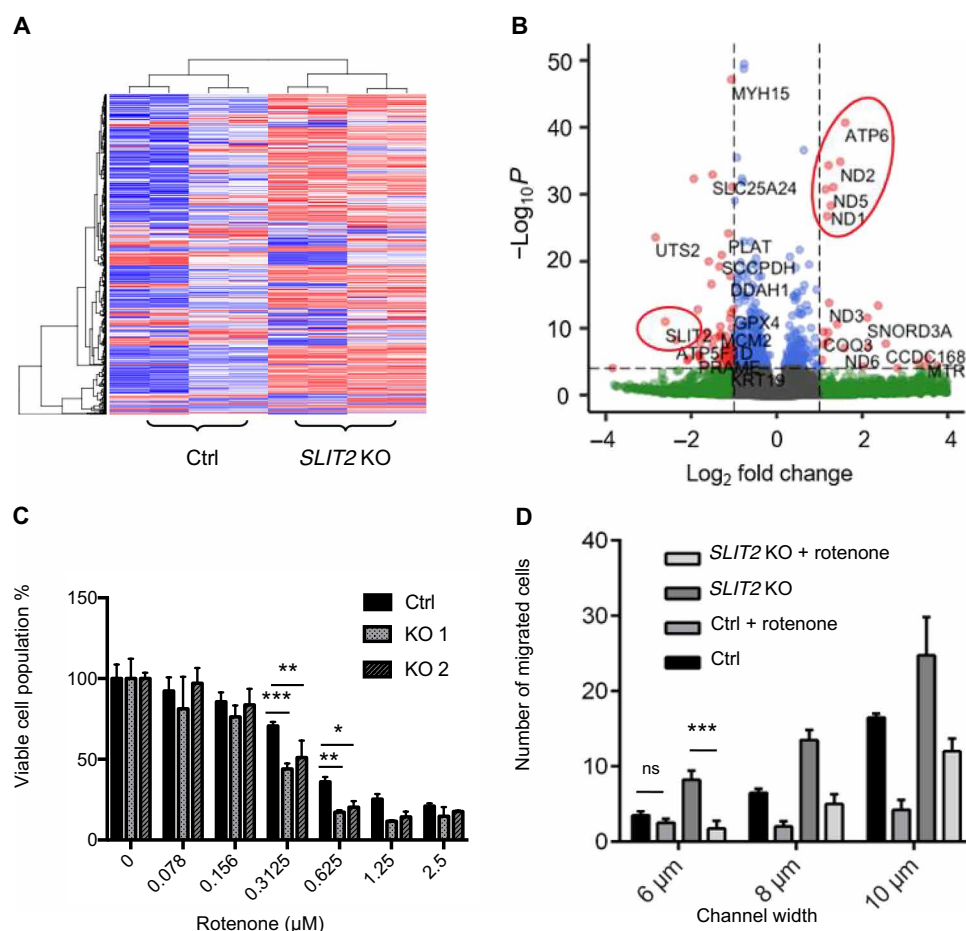

Fig. 6. *SLIT2* KO resulted in elevated complex I expression and hypersensitivity to rotenone. (**A**) Heatmap of the top 1000 differentially expressed genes in *SLIT2* KO cells compared to the NTC control. (**B**) Volcano plot highlighting (in red circles) the most differentially expressed genes of *SLIT2* KO cells compared to NTC. (**C**) Bar graph showing viability of the *SLIT2* KO compared to NTC cells under titration of rotenone (n = 3 for each group). (**D**) Bar graph showing the number of *SLIT2* KO cells migrated across various channel widths compared to the NTC cells, with or without the presence of rotenone at 20% inhibitory concentration (IC$_{20}$) (n = 3 for each group). Error bars indicate SD. *P* values were calculated by two-way ANOVA. ***$P < 0.001$; **$P < 0.01$; *$P < 0.05$; ns, $P > 0.05$.

limited studies on prostate cancer models (*33*, *34*, *36–39*). Promoter hypermethylation was previously found to be responsible for the repression of *SLIT2* and was associated with aggressive prostate, breast, and lung cancers (*33*, *34*). A recent study showed enhanced expression of *SLIT2* in endothelial cells but repressed expression due to hypermethylation in the tumor compartment, suggesting the differential expression profiles of *SLIT2* at the tumor microenvironment as a driver for the release of tumor cells into the blood vessels (*33*). As a top hit in our genome-wide CTC CRISPR KO screen and in a sublibrary screen, *SLIT2* was identified as a strong modulator of invasiveness and metastasis in prostate cancer. The metastasis-promoting effect of *SLIT2* KO was also confirmed in a prostate cancer mouse model in our study. Subcutaneous injection of *SLIT2* KO cells resulted in increased tumor size accompanying marked increase in the number of CTCs in the whole blood compared to the same number of control cells injected. However, a *SLIT2* KO model with similar tumor size as the control group still resulted in significantly increased number of CTCs in the bloodstream, suggesting a possible combined effect of *SLIT2* on dissemination and proliferation. In addition, our study showed enhanced invasive and migratory behavior of *SLIT2* KO cells compared to the control group, suggesting the potential inhibiting effect of *SLIT2* on intravasation and dissemination. However, because metastasis is a very complicated process, the potential roles of *SLIT2* on other pathways that lead to increase in CTC numbers including extravasation and cell viability in the bloodstream could be further studied to comprehensively understand the effect of *SLIT2* on the metastatic process.

No pathways have previously been connected with the invasive behavior of prostate tumor cells carrying a loss-of-function mutation in *SLIT2*, except that the expression of *SLIT2* is regulated by the transcriptional repressor Enhancer of zeste homolog 2 (EZH2) (*34*). Our EMT and transcriptome studies revealed aberrant expression of multiple EMT markers and ETC components in *SLIT2* KO cells that potentially contribute to metastasis. Mitochondrial activity has been linked to cancer progression in various studies (*40–44*), with inhibitors of complex I reported to be promising antineoplastic therapies (*45*, *46*). With the validation of two additional prostate cancer cell lines LNCaP and PC-3, our studies suggest that prostate cancer cells lacking *SLIT2* expression exhibit increased sensitivity toward complex I inhibition, revealing a potential therapeutic strategy for patients with cancer with *SLIT2* loss-of-function mutations.

Bulk sequencing of tumors has uncovered a number of cancer-causing mutations, some of which were harnessed for the development of new targeted therapeutic agents. The identification of gene mutations that are functionally implicated in tumor progression is paramount to nominate new targets for cancer. One important limitation is assessing the function of genes in rare cell populations, such as in CTCs or subsets of immune cells present in the tumor microenvironment. In this study, we performed an in vivo genome-wide CRISPR-Cas9 KO screen targeting CTCs with prostate cancer origin in mouse models. Because the extreme rarity and fragility of patient CTCs resulted in poor feasibility of performing a genome-wide CRISPR screen without extensive ex vivo culturing of the CTCs, we injected a high number of tumor cells into the mice to generate a model to mimic the process of CTC production and to obtain sufficient number of tumor cells from whole mice blood for NGS. Development of this experimental pipeline is transferrable and can be easily applied to search for the unique CTC-promoting factors in other cancer types. Upon establishment of appropriate animal models, this platform can also be further applied to explore genetic factors that affect the behavior of immune cells or other rare cell types in the tumor microenvironment contributing to the metastatic process. Building on this study, we anticipate that combining efficient capture of modeled rare cells with gene editing methodologies will provide new insights into the progression of various diseases, including cancer, and will lead to the imagination of new therapies.

MATERIALS AND METHODS
Cell culture
Prostate cancer cell line PC-3M was obtained from A. Allan at London Health Sciences, London, ON, Canada and was cultured in RPMI 1640 (Wisent). LNCaP and PC-3 were obtained from American Type Culture Collection (ATCC) and cultured in RPMI 1640 and Dulbecco's modified Eagle's medium (DMEM)/F12 (Wisent), respectively. MDA-MB-231 (ATCC) and lenti-X 293T cells (Takara Bio) were grown in DMEM (Sigma-Aldrich) supplemented with 4 mM stable glutamine (Sigma-Aldrich). All culture media were supplemented with 10% fetal bovine serum (FBS) (Wisent) and 1% penicillin/streptomycin (Wisent), and cells were kept at 37°C, 5% CO_2.

Lentiviral production
All lentivirus was produced using lenti-X 293T cells. For TKOv3 genome-wide library production, 8.0 μg of TKOv3 pooled plasmid (Addgene, #90294) (*22*) was cotransfected into 80% confluent lenti-X 293T cells with 4.8 μg of psPAX2 (Addgene, #12260) and 3.2 μg of pMD2.G (Addgene, #12259) per 15-cm plate (Sarstedt). Plasmids psPAX2 and pMD2.G were gifts from Didier Trono. The mixture of plasmids (16.0 μg in 50 μl of ddH_2O) was added to 48 μl of X-tremegene 9 DNA transfection reagents (Roche) that preincubated for 5 min in 750 μl of OptiMEM (Gibco). The mixture of plasmid transfection reagent–OptiMEM was further incubated for 25 min before adding dropwise to lenti-X cells. Eighteen hours later, medium was changed to fresh DMEM. Viral particles were harvested 48 hours after the media exchange, snap-frozen in liquid nitrogen, and stocked at −80°C. The customized sublibrary (plasmid pool synthesized at GenScript) lentivirus was prepared using the same protocol as the TKOv3 library. Individual *SLIT2* CRISPR KO lentivirus was generated following the polyethyenimine transfection protocol (Addgene). sgRNAs targeting the *SLIT2* gene were cloned into the lentiCRISPRv2 (Addgene, #52961) (*47*), and the 20–base pair (bp) sgRNA sequences used were CGG-GTTGGTCTGTACACTCA for KO 1 and ACGGAAAGCTTT-CCTTGGGA for KO 2. For the NTC, the sgRNA sequence used was CCCGAATCTCTATCGTGCGG.

Lentiviral transduction and multiplicity of infection determination
Lentivirus was titrated into 2×10^5 PC-3M cells on six-well plates with 2 ml of complete RPMI 1640 supplemented with polybrene (8 μg/ml; Sigma-Aldrich). After overnight infection, medium was exchanged for fresh RPMI supplemented with puromycin (2 μg/ml; Sigma-Aldrich). After 48 hours of antibiotic selection, multiplicity of infection (MOI) was determined by comparing the number of cells remained at specific viral load with or without puromycin selection using 0.1% crystal violet staining (Sigma-Aldrich) and absorbance reading at 590 nm. A MOI of 0.3 was used for the transduction of CRISPR libraries into the PC-3M cells.

Genome-wide CTC CRISPR KO screen

PC-3M cells (1.0×10^8) were transduced with TKOv3 library (71,090 sgRNAs) at a MOI of 0.3 using polybrene as transduction reagent as described in the previous section. After two rounds of puromycin selection, 3×10^7 transduced cells were subcutaneously injected into the flank of each of the six male athymic nude (nu/nu) mice of 6 to 8 weeks old (1.5×10^7 each side per mouse). Three additional mice were injected with unmodified parental PC-3M cells for tumor size comparison. Tumor volume was measured twice a week using a caliper and calculated using the formula length × width^2/2. Mice were euthanized 3 weeks after transplant to collect tumor and whole blood samples (cardiac puncture). All animal work was conducted following the protocol approved by University of Toronto Animal Care Committee under the guidelines of Canadian Council on Animal Care.

Prism chip design and fabrication

An initial iteration of the Prism chip (24) was modified to increase throughput to 3×10^7 cells/hour per chip and sort cells into zero/low-, medium-, and high-expression outlets. Magnetically labeled cells are deflected laterally on the basis of their level of expression. Deflection is facilitated using guides made from highly magnetically permeable alloy set at an angle from the fluid flow (5° for medium and 20° for high). In the presence of a magnetic field from a permanent magnet, localized regions of high magnetic flux are found at guide edges causing the attraction of magnetic nanoparticles (48). A balancing of the magnetic force and the Stokes drag force from fluid flow causes magnetically labeled cells to follow the deflection guides until the angle changes or the guides end at the lateral edges of the device. Angle changes of the guides cause an increase in the component of the drag force and medium-expression cells to detach. Chips were fabricated on a soda lime glass wafer (UniversityWafer). Guides were patterned using photolithography and wet etching, and channels were created using SU-8 photo resist (Kayaku AM). A polydimethylsiloxane (PDMS) slab (Dow Sylgard) was bonded to encapsulate the device according to an existing protocol (49). Multiple chips were set up in parallel to simultaneously isolate CTCs from multiple blood samples. To prepare the Prism chips for CTC isolation, the chips were primed with sterile water containing 0.1% Pluronic F68 (Sigma-Aldrich) under constant hydraulic pressure for overnight before use. The nonionic surfactant Pluronic F68 prevented nonspecific capture of cells in the microchannel, and the constant hydraulic pressure removed small air bubbles. For immunomagnetic-based cell sorting, the Prism chip was first mounted on a permanent magnet (BY088-N52, K&J Magnetics). Before sample loading, a buffer solution made of Hanks' balanced salt solution (HBSS; GIBCO) supplemented with 2% bovine serum albumin (BSA; Sigma-Aldrich) and 5 mM EDTA (BioShop) was introduced to the Prism chip to remove the pluronic water.

CTC collection and cell lysis

To isolate the CTCs, each blood sample was diluted in a 1:1 ratio with the HBSS buffer solution and incubated with 10% EpCAM MicroBeads (Miltenyi Biotec) with shaking at room temperature for an hour. Afterward, equal volumes of buffer solution and the blood samples containing the magnetically labeled CTCs were loaded onto the buffer inlet and sample inlet, respectively, before withdrawn from the chip at a flow rate of 2 ml/hour. After sample processing, 300 µl of buffer solution was loaded to both the sample and buffer inlets and withdrawn at the same flow rate to wash out remaining samples in the microchannels. Solution collected from the high-expression outlet (~500 µl) of each chip was injected into a 1.5 ml centrifuge microtube (Axygen) and set on the DynaMag-2 magnet (Thermo Fisher Scientific) for an hour. After the cells settled down, supernatant was pipetted out slowly without touching the bottom or the wall of the tube, leaving minimal solution (5 to 10 µl) containing CTCs. Alkaline lysis method adapted from a previous publication was used to lyse CTCs (25). Briefly, 10 µl of 200 mM KOH with 50 mM dithiothreitol was added to CTC solution and heated at 65°C for 10 min in a thermocycler. Lysate was then neutralized by 10 µl of 900 mM tris-HCl (pH 8.3) with 300 mM KCl and 200 mM HCl.

Genomic DNA extraction and PCR amplification of sgRNA

To extract gDNA from the CRISPR library–transduced cell pool (3×10^7 to 5×10^7 cells) and the tumor tissues (100 to 200 mg), the QIAamp DNA Blood Maxi Kit (Qiagen) was used following the manufacturer's instructions. For gDNA extraction from tumor tissues, tumors were chopped into small pieces using a razor blade and incubated with 1.8-ml tissue lysis buffer ATL (Qiagen) and 0.2 ml of proteinase K (Qiagen) at 56°C overnight before processed using the QIAamp DNA Blood Maxi Kit. gDNA extracted from the initial cell pool, and the primary tumor samples were checked for 230:280 and 260:280 ratios before sending to the Princess Margret Genomics Center (PMGC; Toronto, ON, Canada) for PCR amplification of the sgRNA region and generation of the barcoded sgRNA library. For the CTC samples, gDNA extraction was not necessary, and 10 µl of the neutralized lysate from each CTC sample was directly set for PCR amplification of the sgRNA region. Each 100 µl of PCR was set as follows: 10 µl of 10× buffer (supplied with Ex Taq), 8 µl of deoxynucleotide triphosphate (supplied with Ex Taq), 5 µl of Amp1 primer mix (10 µM), 10 µl of neutralized CTC lysate, 65.5 µl of water, and 1.5 µl of Ex Taq DNA polymerase (Takara Bio).

The thermocycling parameters used were as follows: Step 1: 95°C for 1 min; step 2: 95°C for 30 s; step 3: 52°C for 30 s; step 4: 72°C for 20 s (repeat steps 2 to 4 for 34 additional times); step 5: 72°C for 2 min; step 6: 4°C hold. PCR products were run on a 1% agarose gel to confirm the size of the product (expected size: 235 bp) before sent to PMGC for barcoded sgRNA library generation. NGS was done using Illumina NovaSeq 6000 with 1 million reads per sample.

CTC subpool CRISPR KO screen

Sublibrary (400 sgRNAs) was synthesized and cloned into the same vector as the TKOv3 genome-wide library (lentiCRISPRv2) by GenScript. Cloned sublibrary was deep-sequenced to verify sgRNA representation in the plasmid pool. Lentivirus production, MOI determination, and in vivo screen were conducted in the same manner as the TKOv3 library, except that GPI-anchored tag was lentivirally introduced to the PC-3M cells for displaying Myc on the cell surface before introducing the sublibrary to the cells. Thus, CTCs in blood samples were labeled with 1% biotinylated anti-Myc antibody (Abcam, ab197139) for an hour and 5% anti-biotin microbeads (Miltenyi Biotech) for an hour before being isolated on the Prism chip. Lysis and sgRNA PCR amplification of CTCs in the sublibrary screen used the same protocol as the genome-wide screen.

NGS data and sgRNA enrichment analyses

The genome-wide screen data were mapped by PMGC, and the customized sublibrary data were mapped following the MAGeCK

pipeline (50). Number of reads in each sample was normalized by converting raw sgRNA counts to reads per million (rpm). The rpm values were then subject to $\log_2$ transformation for downstream analyses. To generate correlation heatmaps, Nonnegative matrix factorization (NMF) R package was used (51), and Pearson correlations between individual samples were calculated using $\log_2$ rpm counts. Empirical cumulative distribution plot was generated using the Python libraries Pandas, Seaborn, and Matplotlib. Biological pathway enrichment analysis was performed using Metascape (52). For sgRNA enrichment analysis, fold change was obtained using MAGeCK and two criteria were used to identify the top candidate genes from the genome-wide screen based on CTC sgRNAs: (i) counts: if a sgRNA was counted as the top 100 in the normalized mapping results of any CTC sample (100 sgRNAs × 6 replicates), resulting in 162 unique sgRNAs instead of 600 due to the exclusion of the overlapping sgRNAs among the six replicates; (ii) replicates: if a CTC sgRNA was enriched compared to its counterpart in the corresponding primary tumor sample (fold change $\geq$ 1.0) across all the samples ($n = 6$). For the sublibrary data, sgRNA counts were normalized and analyzed for enrichment using DrugZ (53).

In vivo validation of screen top hit

PC-3M NTC or *SLIT2* KO cells (1.0×10^6 each) were orthotopically injected into the prostate via the right dorsolateral lobe of 6- to 8-week-old male athymic nude (nu/nu) mice. After 3 weeks, mice were euthanized to collect primary tumor (size comparison), blood (CTC counting), and lymph nodes (metastasis histology). Peripheral lymph nodes from the mice were collected, including two inguinal, two axillary, and two brachial lymph nodes from each mouse. Lymph nodes for histology were formalin-fixed, paraffin-embedded, sectioned, and stained with H&E (prepared by Pathology Research Program Laboratory at University Healthy Network). Prepared tissue sections were imaged and examined by a pathologist at Charles River Laboratories for the assessment and grading of the metastatic lesions. The metastatic status of the lymph nodes was categorized into three groups: no neoplastic cells observed inside the lymph nodes or at the peripheral tissues (none); neoplastic cells observed inside the lymph nodes or at the peripheral tissues (partial); and neoplastic cells observed inside the lymph nodes and constituted greater than half of the cross-sectional area (severe).

Fabrication and performance of the eight-zone CTC capture device

Eight-zone profiling chips were fabricated using 3D stereolithography for the 3D-printed molds and standard soft lithographic techniques for subsequent steps as described previously (54–56). Before usage, the microfluidic chips were treated with 0.1% Pluronic F-68 overnight. Devices were assembled with two rectangular arrays of N52 neodymium magnets above and below before connected to a syringe pump (Chemyx) set to withdraw for the duration of the sample processing. Blood samples were prepared following the same protocol as for the Prism chips before loaded onto the eight-zone device, and CTCs were captured and profiled for EpCAM expression. Phosphate-buffered saline (PBS; 500 µl) was withdrawn through the chip to displace the Pluronic F-68 solution before sample loading. The samples were processed at a flow rate of 750 µl/hour. The samples were then fixed with 150 µl of 4% paraformaldehyde (Sigma-Aldrich) in PBS, permeabilized with 150 µl of 0.2% Triton X-100 (Sigma-Aldrich) in PBS. The chips were washed in between

each step with 125 µl of CliniMACS PBS-EDTA solution (Miltenyi). Captured cells were immunostained by 200 µl of an antibody cocktail containing anti-pan cytokeratin AF488 (30 µg/ml; Abcam, ab277270), anti-cytokeratin 18 fluorescein isothiocyanate (6 µg/ml; LifeSpan BioSciences, LS-C46335), anti-cytokeratin 19 AF488 (30 µg/ml; BioLegend, 628508), and anti-mouse CD45 fluorophore Allophyco-cyanin (3 µg/ml; BD Bioscience, 559864) in PBS supplemented with 1% BSA and 0.1% Tween 20 (Sigma-Aldrich) at a flow rate of 200 µl/hour. The captured cells were then stained with 4′,6-diamidino-2-phenylindole (Thermo Fisher Scientific, R37606) before fluorescently imaged and scanned using a Nikon Ti-E Eclipse microscope with Andor's Neo sCMOS camera. CTCs were identified as nucleus present and EpCAM$^+$ CK$^+$ CD45$^-$ cells.

Spheroid assay

3D spheroids consisting of NTC or *SLIT2* KO cells were grown following a protocol described previously (57). Briefly, RPMI 1640 was supplemented with 0.75% methylcellulose (Sigma-Aldrich), and the spheroids were cultured in pretreated ultralow attachment plates (Corning). To determine the amount of cells consisting the spheroids in each well, CellTiter-Glo 3D Cell Viability Assay (Promega) was used following the manufacturer's instructions. Briefly, assay reagent was mixed vigorously with cell culture medium at a 1-to-1 ratio after the plate was brought to room temperature. After 25 min of incubation at room temperature, luminescence was recorded for each well.

Migration chip fabrication and cell migration/ deformability assay

The migration chip includes a sample-loading channel in the middle and two stimulus-loading channels on each side. There are numerous narrow migration channels (constant height at 5 µm) with varying widths ranging from 6 to 20 µm connecting the sample channel and stimulation channels for cell migration. The chip consists of a PDMS substrate with microchannels and a glass cover. The PDMS substrate was fabricated using soft lithography. Briefly, the liquid base and reagent of PDMS were fully mixed at a ratio of 10:1, casted on a SU8-negative photoresist-patterned silicon mold, and then incubated at 70°C for 2 hours for polymerization. The solidified PDMS was peeled off the mold and bonded with the glass cover upon plasma treatment. For cell deformability assay, the migration chip was first filled with 70% ethanol and ultraviolet-treated. The degassed and sterilized chip was then washed with PBS followed by cell culture medium. PC-3M NTC (3×10^6) or *SLIT2* KO cells in 500 µl of complete medium were loaded to the sample channel and incubated at 37°C for overnight to allow cell attachment. The next day, the sample channel was washed with PBS and loaded with serum-free medium. The stimulus channels were filled with fresh cell culture medium with 10% FBS to produce nutrient gradient along the narrow migration channels. After 6 hours of incubation, cells across the entire chip were fluorescently labeled by loading 5 µM SYTO 24 (Invitrogen) to both the sample and stimulation channels and incubated for 15 min. Migration behavior of the cells were inspected under a fluorescence microscope. Cells that entered the migration channels or reached the stimulus channels were considered as deformed and migrated cells. The number of migrated cells was counted and compared for the deformability and migration potential of the cells from different samples. For testing the effect of rotenone on deformability and migration of the cells, rotenone at 20% inhibitory concentration (IC_{20}) was added to the medium loaded onto the chip.

Transcell cell invasion assay

To prepare the invasion assay chambers, 750 μl of 10% FBS-supplemented RPMI 1640 was added to each of the 24 wells of the Transwell plate (Corning), and 100 μl of Matrigel (Corning) was added to the cell culture inserts (8 μm). The plate was incubated in a humidified incubator at 37°C with 5% CO_2 for an hour. Five hundred microliters of PC-3M NTC or *SLIT2* KO cells in serum-free RPMI 1640 was added to the Matrigel-coated inserts at 1×10^5 cells/ml. On the basis of the conditions tested, medium in the wells was either with or without 10% FBS and secreted N-SLIT2 (1 μg/ml; R&D Systems, 8616-SL-050). The cells were incubated in the Matrigel-coated inserts for overnight in the incubator. The next day, medium was removed from the inserts and wells. The nonmigrated cells on the upper side of the membrane were removed using a cotton swab and washed away with PBS. Cells that remained on the membrane were fixed by submerging the membranes in the wells filled with cold methanol for 20 min and air-dried for 30 min. The membranes were then submerged in 750 μl of 0.1% crystal violet (Sigma-Aldrich) in wells for 30 min at room temperature to stain the cells before washed thoroughly with distilled water. After air-drying, membranes were submerged in 750 μl of 10% acetic acid (VWR) with shaking until the stain was completely dissolved. Optical density of the dissolved stain in each well was determined at 590 nm using a microplate reader.

Oncology proteome antibody array

Oncology antibody array (R&D Systems) was performed following the manufacturer's instructions. Briefly, NTC or *SLIT2* KO cell lysates were diluted and incubated overnight with the nitrocellulose membranes that had been prespotted in duplicate with antibodies targeting 84 oncology-related proteins. The membranes were washed before incubated with a cocktail of biotinylated detection antibodies, followed by addition of streptavidin–horseradish peroxidase. The amount of protein bound at each capture spot was detected using a chemiluminescent substrate, and the signal was captured using a ChemiDoc imaging system (Bio-Rad). Intensity of the capture spots was quantified using ImageJ.

Immunoblot analysis

Whole-cell extracts were prepared with radioimmunoprecipitation assay buffer (Thermo Fisher Scientific) supplemented with protease inhibitor cocktail (Sigma-Aldrich). Proteins were separated on 4 to 15% precast protein gels (Bio-Rad) and transferred onto polyvinylidene difluoride membranes. Primary antibodies used were anti-SLIT2 (Abcam, ab134166), anti-Vimentin (Abcam, ab92547), anti–N-cadherin (BD Bioscience, 610920), anti–E-cadherin (R&D Systems, AF648), and anti-Snail (NEB, 3879S). Secondary antibodies were purchased from Cell Signaling Technology. Blots were visualized with chemiluminescent substrate (Thermo Fisher Scientific) using a ChemiDoc imaging system. Intensity of the protein bands were quantified using ImageJ.

RNA sequencing and data analysis

RNA was extracted using the RNeasy Plus Kit (Qiagen) following the manufacturer's instructions and submitted to PMGC for complementary DNA library preparation and RNA sequencing using Illumina NovaSeq 6000. RNA sequencing data was processed for sgRNA representation using A*STAR procedure. Figures were generated using the normalized read counts in R and RStudio (R project, Revolution Analytics), Metascape, and the Gene Set Enrichment Analysis tools (Broad Institute).

Cell viability assay

NTC or *SLIT2* KO PC-3M cells were seeded on 96-well plates in triplicate at a density of 2×10^4 cells per well. The next day, rotenone was titrated into the 96-well plate at twofold serial dilution with concentration ranging from 0 to 10 μM. Viable cell population was determined 48 hours later using the Cell Counting Kit-8 (Dojindo) following the manufacturer's instructions.

Clinical and patient data analysis

RNA sequencing and clinical data were retrieved from portals of TCGA, the Human Protein Atlas, GEPIA2, and COSMIC. *SLIT2* expression median of 2.45 Fragments Per Kilobase Million (FPKM) was used as the threshold to define low or high expression of *SLIT2* in patients with prostate cancer (prostate adenocarcinoma). *SLIT2* expression levels in tumor and normal tissues were retrieved for 31 cancer types to assess fold change. Information on the loss-of-function mutations in the top screen hits occurred in patients with cancer was retrieved from Cancer Mutation Census (CMC) at COSMIC to compare with the level of loss-of-function mutations in well-known TSGs and OGs (29).

Data collection and analysis

Counts of sgRNAs were collected by PMGC Toronto and analyzed using MAGeCK or DrugZ as described above. Screen data quality control analysis and figure preparations were performed using software packages as specified in the corresponding sections above. Microscopy images were acquired using Zeiss Axio Observer and prepared using Zeiss Zen Blue. Protein band intensities were analyzed and quantified using ImageJ. Biological pathway analysis was performed using Metascape. Data were analyzed using the statistical tests with specified sample sizes indicated in each figure legend. Statistical tests and graphic representation of the data were conducted using Graphpad Prism v7.0. All data were presented as the mean with SD indicated by error bars. Statistical significance was set at $P < 0.05$ with two-sided tests.

SUPPLEMENTARY MATERIALS

Supplementary material for this article is available at https://science.org/doi/10.1126/sciadv.abo7792

View/request a protocol for this paper from *Bio-protocol*.

REFERENCES AND NOTES

1. P. S. Steeg, Tumor metastasis: Mechanistic insights and clinical challenges. *Nat. Med.* **12**, 895–904 (2006).
2. C. L. Chaffer, R. A. Weinberg, A perspective on cancer cell metastasis. *Science* **331**, 1559–1564 (2011).
3. J. Fares, M. Y. Fares, H. H. Khachfe, H. A. Salhab, Y. Fares, Molecular principles of metastasis: A hallmark of cancer revisited. *Signal Transduct. Target. Ther.* **5**, 28 (2020).
4. R. L. Siegel, K. D. Miller, A. Jemal, Cancer statistics, 2020. *CA Cancer J. Clin.* **70**, 7–30 (2020).
5. K. Ganesh, J. Massagué, Targeting metastatic cancer. *Nat. Med.* **27**, 34–44 (2021).
6. P. Priestley, J. Baber, M. P. Lolkema, N. Steeghs, E. de Bruijn, C. Shale, K. Duyvesteyn, S. Haidari, A. van Hoeck, W. Onstenk, P. Roepman, M. Voda, H. J. Bloemendal, V. C. G. Tjan-Heijnen, C. M. L. van Herpen, M. Labots, P. O. Witteveen, E. F. Smit, S. Sleijfer, E. E. Voest, E. Cuppen, Pan-cancer whole-genome analyses of metastatic solid tumours. *Nature* **575**, 210–216 (2019).
7. H. Beltran, K. Eng, J. M. Mosquera, A. Sigaras, A. Romanel, H. Rennert, M. Kossai, C. Pauli, B. Faltas, J. Fontugne, K. Park, J. Banfelder, D. Prandi, N. Madhukar, T. Zhang, J. Padilla, N. Greco, T. J. McNary, E. Herrscher, D. Wilkes, T. Y. MacDonald, H. Xue, V. Vacic, A. K. Emde, D. Oschwald, A. Y. Tan, Z. Chen, C. Collins, M. E. Gleave, Y. Wang, D. Chakravarty, M. Schiffman, R. Kim, F. Campagne, B. D. Robinson, D. M. Nanus, S. T. Tagawa, J. Z. Xiang, A. Smogorzewska, F. Demichelis, D. S. Rickman, A. Sboner, O. Elemento, M. A. Rubin, Whole-exome sequencing of metastatic cancer and biomarkers of treatment response. *JAMA Oncol.* **1**, 466–474 (2015).

8. S. Vignot, B. Besse, F. André, J. P. Spano, J. C. Soria, Discrepancies between primary tumor and metastasis: A literature review on clinically established biomarkers. *Crit. Rev. Oncol. Hematol.* **84**, 301–313 (2012).

9. S. Turajlic, C. Swanton, Metastasis as an evolutionary process. *Science* **352**, 169–175 (2016).

10. J. G. Lohr, V. A. Adalsteinsson, K. Cibulskis, A. D. Choudhury, M. Rosenberg, P. Cruz-Gordillo, J. M. Francis, C. Zhang, A. K. Shalek, R. Satija, J. J. Trombetta, D. Lu, N. Tallapragada, N. Tahirova, S. Kim, B. Blumenstiel, C. Sougnez, A. Lowe, B. Wong, D. Auclair, E. M. van Allen, M. Nakabayashi, R. T. Lis, G. M. Lee, T. Li, M. S. Chabot, A. Ly, M. Taplin, T. E. Clancy, M. Loda, A. Regev, M. Meyerson, W. C. Hahn, P. W. Kantoff, T. R. Golub, G. Getz, J. S. Boehm, J. C. Love, Whole-exome sequencing of circulating tumor cells provides a window into metastatic prostate cancer. *Nat. Biotechnol.* **32**, 479–484 (2014).

11. E. Rossi, R. Zamarchi, Single-cell analysis of circulating tumor cells: How far have we come in the-omics era? *Front. Genet.* **7**, 958 (2019).

12. C. Alix-Panabières, K. Pantel, Challenges in circulating tumour cell research. *Nat. Rev. Cancer* **14**, 623–631 (2014).

13. V. Ortiz, M. Yu, Analyzing circulating tumor cells one at a time. *Trends Cell Biol.* **28**, 764–775 (2018).

14. Z. Zhu, S. Qiu, K. Shao, Y. Hou, Progress and challenges of sequencing and analyzing circulating tumor cells. *Cell Biol. Toxicol.* **34**, 405–415 (2018).

15. M. Labib, S. O. Kelley, Circulating tumor cell profiling for precision oncology. *Mol. Oncol.* **15**, 1622–1646 (2021).

16. A. Babayan, M. Alawi, M. Gormley, V. Müller, H. Wikman, R. P. McMullin, D. A. Smirnov, W. Li, M. Geffken, K. Pantel, S. A. Joosse, Comparative study of whole genome amplification and next generation sequencing performance of single cancer cells. *Oncotarget* **8**, 56066–56080 (2017).

17. S. Chen, N. E. Sanjana, K. Zheng, O. Shalem, K. Lee, X. Shi, D. A. Scott, J. Song, J. Q. Pan, R. Weissleder, H. Lee, F. Zhang, P. A. Sharp, Genome-wide CRISPR screen in a mouse model of tumor growth and metastasis. *Cell* **160**, 1246–1260 (2015).

18. R. Y. Ebright, S. Lee, B. S. Wittner, K. L. Niederhoffer, B. T. Nicholson, A. Bardia, S. Truesdell, D. F. Wiley, B. Wesley, S. Li, A. Mai, N. Aceto, N. Vincent-Jordan, A. Szabolcs, B. Chirn, J. Kreuzer, V. Comaills, M. Kalinich, W. Haas, D. T. Ting, M. Toner, S. Vasudevan, D. A. Haber, S. Maheswaran, D. S. Micalizzi, Deregulation of ribosomal protein expression and translation promotes breast cancer metastasis. *Science* **367**, 1468–1473 (2020).

19. N. Carmona-Ule, M. González-Conde, C. Abuín, J. F. Cueva, P. Palacios, R. López-López, C. Costa, A. B. Davila-Ibáñez, Short-term ex vivo culture of CTCs from advance breast cancer patients: Clinical implications. *Cancers* **13**, 2668 (2021).

20. S. Sharma, R. Zhuang, M. Long, M. Pavlovic, Y. Kang, A. Ilyas, W. Asghar, Circulating tumor cell isolation, culture, and downstream molecular analysis. *Biotechnol. Adv.* **36**, 1063–1078 (2018).

21. R. D. Chow, S. Chen, Cancer CRISPR screens in vivo. *Trends Cancer* **4**, 349–358 (2018).

22. T. Hart, A. H. Y. Tong, K. Chan, J. Van Leeuwen, A. Seetharaman, M. Aregger, M. Chandrashekhar, N. Hustedt, S. Seth, A. Noonan, A. Habsid, O. Sizova, L. Nedyalkova, R. Climie, L. Tworzyanski, K. Lawson, M. A. Sartori, S. Alibeh, D. Tieu, S. Masud, P. Mero, A. Weiss, K. R. Brown, M. Usaj, M. Billmann, M. Rahman, M. Constanzo, C. L. Myers, B. J. Andrews, C. Boone, D. Durocher, J. Moffat, Evaluation and design of genome-wide CRISPR/SpCas9 knockout screens. *G3* **7**, 2719–2727 (2017).

23. B. Mair, P. M. Aldridge, R. S. Atwal, D. Philpott, M. Zhang, S. N. Masud, M. Labib, A. H. Y. Tong, E. H. Sargent, S. Angers, J. Moffat, S. O. Kelley, High-throughput genome-wide phenotypic screening via immunomagnetic cell sorting. *Nat. Biomed. Eng.* **3**, 796–805 (2019).

24. P. M. Aldridge, M. Mukhopadhyay, S. U. Ahmed, W. Zhou, E. Christinck, R. Makonnen, E. H. Sargent, S. O. Kelley, Prismatic deflection of live tumor cells and cell clusters. *ACS Nano* **12**, 12692–12700 (2018).

25. S. A. Kim, J. A. Yoon, M. J. Kang, Y. M. Choi, S. J. Chae, S. Y. Moon, An efficient and reliable DNA extraction method for preimplantation genetic diagnosis: A comparison of allele drop out and amplification rates using different single cell lysis methods. *Fertil. Steril.* **92**, 814–818 (2009).

26. J. Brugarolas, K. Lei, R. L. Hurley, B. D. Manning, J. H. Reiling, E. Hafen, L. A. Witters, L. W. Ellisen, W. G. Kaelin Jr., Regulation of mTOR function in response to hypoxia by REDD1 and the TSC1/TSC2 tumor suppressor complex. *Genes Dev.* **18**, 2893–2904 (2004).

27. K. Inoki, Y. Li, T. Zhu, J. Wu, K. Guan, TSC2 is phosphorylated and inhibited by Akt and suppresses mTOR signalling. *Nat. Cell Biol.* **4**, 648–657 (2002).

28. Z. Sondka, S. Bamford, C. G. Cole, S. A. Ward, I. Dunham, S. A. Forbes, The COSMIC Cancer Gene Census: Describing genetic dysfunction across all human cancers. *Nat. Rev. Cancer* **18**, 696–705 (2018).

29. F. Sanchez-Vega, M. Mina, J. Armenia, W. K. Chatila, A. Luna, K. C. La, S. Dimitriadoy, D. L. Liu, H. S. Kantheti, S. Saghafinia, D. Chakravarty, F. Daian, Q. Gao, M. H. Bailey, W. W. Liang, S. M. Foltz, I. Shmulevich, L. Ding, Z. Heins, A. Ochoa, B. Gross, J. Gao, H. Zhang, R. Kundra, C. Kandoth, I. Bahceci, L. Dervishi, U. Dogrusoz, W. Zhou, H. Shen,

P. W. Laird, G. P. Way, C. S. Greene, H. Liang, Y. Xiao, C. Wang, A. Iavarone, A. H. Berger, T. G. Bivona, A. J. Lazar, G. D. Hammer, T. Giordano, L. N. Kwong, G. McArthur, C. Huang, A. D. Tward, M. J. Frederick, F. McCormick, M. Meyerson, C. G. A. R. Network, E. M. van Allen, A. D. Cherniack, G. Ciriello, C. Sander, N. Schultz, Oncogenic signaling pathways in the cancer genome atlas. *Cell* **173**, 321–337.e10 (2018).

30. J. M. Rothberg, D. A. Hartley, Z. Walther, S. Artavanis-Tsakonas, slit: An EGF-homologous locus of *D. melanogaster* involved in the development of the embryonic central nervous system. *Cell* **55**, 1047–1059 (1988).

31. M. A. Manavalan, V. R. Jayasinghe, R. Grewal, K. M. Bhat, The glycosylation pathway is required for the secretion of Slit and for the maintenance of the Slit receptor Robo on axons. *Sci. Signal.* **10**, eaam5841 (2017).

32. L. J. Wang, Y. Zhao, H. Bing, Y. Ma, J. Zhang, D. Yang, J. Mao, F. Tang, W. Li, Y. Yang, R. Wang, J. Geng, Targeting Slit-Roundabout signaling inhibits tumor angiogenesis in chemical-induced squamous cell carcinogenesis. *Cancer Sci.* **99**, 510–517 (2008).

33. B. Tavora, T. Mederer, K. J. Wessel, S. Ruffing, M. Sadjadi, M. Missmahl, B. N. Ostendorf, X. Liu, J. Y. Kim, O. Olsen, A. L. Welm, H. Goodarzi, S. F. Tavazoie, Tumoural activation of TLR3-SLIT2 axis in endothelium drives metastasis. *Nature* **586**, 299–304 (2020).

34. J. Yu, Q. Cao, J. Yu, L. Wu, A. Dallol, J. Li, G. Chen, C. Grasso, X. Cao, R. J. Lonigro, S. Varambally, R. Mehra, N. Palanisamy, J. Y. Wu, F. Latif, A. M. Chinnaiyan, The neuronal repellent SLIT2 is a target for repression by EZH2 in prostate cancer. *Oncogene* **29**, 5370–5380 (2010).

35. L. Kermanshah, M. Poudineh, A. Ahmed, L. N. M. Nguyen, S. Srikant, R. Makonnen, F. P. Cantu, M. Corrigan, S. O. Kelley, Dynamic CTC phenotypes in metastatic prostate cancer models visualized using magnetic ranking cytometry. *Lab Chip* **18**, 2055–2064 (2018).

36. T. L. Bartholow, M. J. Becich, U. R. Chandran, A. V. Parwani, Immunohistochemical staining of Slit2 in primary and metastatic prostatic adenocarcinoma. *Transl. Oncol.* **4**, 314–320 (2011).

37. M. Tong, T. Jun, Y. Nie, J. Hao, D. Fan, The role of the SLIT/Robo signaling pathway. *J. Cancer* **10**, 2694–2705 (2019).

38. Z. Jiang, G. Liang, Y. Xiao, T. Qin, X. Chen, E. Wu, Q. Ma, Z. Wang, Targeting the SLIT/ROBO pathway in tumor progression: Molecular mechanisms and therapeutic perspectives. *Ther. Adv. Med. Oncol.* **11**, 1758835919855238 (2019).

39. M. J. Jeon, M. Lim, M.-h. You, J. Park, D. E. Song, D. Sim, T. Y. Kim, Y. K. Shong, W. B. Kim, W. G. Kim, The role of Slit2 as a tumor suppressor in thyroid cancer. *Mol. Cell. Endocrinol.* **483**, 87–96 (2019).

40. P. E. Porporato, V. L. Payen, J. Pérez-Escuredo, C. J. De Saedeleer, P. Danhier, T. Copetti, S. Dhup, M. Tardy, T. Vazeille, C. Bouzin, O. Feron, C. Michiels, B. Gallez, P. Sonveaux, A mitochondrial switch promotes tumor metastasis. *Cell Rep.* **8**, 754–766 (2014).

41. P. E. Porporato, N. Filigheddu, J. M. B. S. Pedro, G. Kroemer, L. Galluzzi, Mitochondrial metabolism and cancer. *Cell Res.* **28**, 265–280 (2018).

42. A. D. Scheid, T. C. Beadnell, D. R. Welch, Roles of mitochondria in the hallmarks of metastasis. *Br. J. Cancer* **124**, 124–135 (2021).

43. B. Bhandary, A. Marahatta, H. R. Kim, H. J. Chae, Mitochondria in relation to cancer metastasis. *J. Bioenerg. Biomembr.* **44**, 623–627 (2012).

44. V. S. Lebleu, J. T. O'Connell, K. N. Gonzalez Herrera, H. Wikman, K. Pantel, M. C. Haigis, F. M. De Carvalho, A. Damascena, L. T. Domingos Chinen, R. M. Rocha, J. M. Asara, R. Kalluri, PGC-1α mediates mitochondrial biogenesis and oxidative phosphorylation in cancer cells to promote metastasis. *Nat. Cell Biol.* **16**, 992–1003 (2014).

45. F. A. Urra, F. Muñoz, A. Lovy, C. Cárdenas, The mitochondrial Complex(I)ty of cancer. *Front. Oncol.* **7**, 118 (2017).

46. A. Naguib, G. Mathew, C. R. Reczek, K. Watrud, A. Ambrico, T. Herzka, I. C. Salas, M. F. Lee, N. El-Amine, W. Zheng, M. E. Di Francesco, J. R. Marszalek, D. J. Pappin, N. S. Chandel, L. C. Trotman, Mitochondrial complex i inhibitors expose a vulnerability for selective killing of Pten-Null cells. *Cell Rep.* **23**, 58–67 (2018).

47. N. E. Sanjana, O. Shalem, F. Zhang, Improved vectors and genome-wide libraries for CRISPR screening. *Nat. Methods* **11**, 783–784 (2014).

48. S. S. Shevkoplyas, A. C. Siegel, R. M. Westervelt, M. G. Prentiss, G. M. Whitesides, The force acting on a superparamagnetic bead due to an applied magnetic field. *Lab Chip* **7**, 1294–1302 (2007).

49. D. Philpott, P. Aldridge, B. Mair, R. Atwal, S. Masud, M. Zhang, A. Tong, E. Sargent, S. Angers, J. Moffat, S. Kelley, High-throughput microfluidic cell sorting platform (MICS). *Protoc. Exch.* 10.21203/rs.2.10282/v1, (2019).

50. B. Wang, M. Wang, W. Zhang, T. Xiao, C. Chen, A. Wu, F. Wu, N. Traugh, X. Wang, Z. Li, S. Mei, Y. Cui, S. Shi, J. J. Lipp, M. Hinterndorfer, J. Zuber, M. Brown, W. Li, X. S. Liu, Integrative analysis of pooled CRISPR genetic screens using MAGeCKFlute. *Nat. Protoc.* **14**, 756–780 (2019).

51. R. Gaujoux, C. Seoighe, A flexible R package for nonnegative matrix factorization. *BMC Bioinformatics* **11**, 367 (2010).

52. Y. Zhou, B. Zhou, L. Pache, M. Chang, A. H. Khodabakhshi, O. Tanaseichuk, C. Benner, S. K. Chanda, Metascape provides a biologist-oriented resource for the analysis of systems-level datasets. *Nat. Commun.* **10**, 1523 (2019).

53. M. Colic, G. Wang, M. Zimmermann, K. Mascall, M. McLaughlin, L. Bertolet, W. F. Lenoir, J. Moffat, S. Angers, D. Durocher, T. Hart, Identifying chemogenetic interactions from CRISPR screens with drugZ. *Genome Med.* **11**, 52 (2019).

54. M. Labib, Z. Wang, S. U. Ahmed, R. M. Mohamadi, B. Duong, B. Green, E. H. Sargent, S. O. Kelley, Tracking the expression of therapeutic protein targets in rare cells by antibody-mediated nanoparticle labelling and magnetic sorting. *Nat. Biomed. Eng.* **5**, 41–52 (2021).

55. B. T. V. Duong, L. Wu, B. J. Green, F. Bavaghar-Zaeimi, Z. Wang, M. Labib, Y. Zhou, F. J. P. Cantu, T. Jeganathan, S. Popescu, J. Pantea, M. de Perrot, S. O. Kelley, A liquid biopsy for detecting circulating mesothelial precursor cells: A new biomarker for diagnosis and prognosis in mesothelioma. *EBioMedicine* **61**, 103031 (2020).

56. Z. Wang, M. Gagliardi, R. M. Mohamadi, S. U. Ahmed, M. Labib, L. Zhang, S. Popescu, Y. Zhou, E. H. Sargent, G. M. Keller, S. O. Kelley, Ultrasensitive and rapid quantification of rare tumorigenic stem cells in hPSC-derived cardiomyocyte populations. *Sci. Adv.* **6**, eaay7629 (2020).

57. K. Han, S. E. Pierce, A. Li, K. Spees, G. R. Anderson, J. A. Seoane, Y. H. Lo, M. Dubreuil, M. Olivas, R. A. Kamber, M. Wainberg, K. Kostyrko, M. R. Kelly, M. Yousefi, S. W. Simpkins, D. Yao, K. Lee, C. J. Kuo, P. K. Jackson, A. Sweet-Cordero, A. Kundaje, A. J. Gentles, C. Curtis, M. M. Winslow, M. C. Bassik, CRISPR screens in cancer spheroids identify 3D growth-specific vulnerabilities. *Nature* **580**, 136–141 (2020).